Article

Low-Temperature Deformation and Fracture of Cr-Mn-N Stainless Steel: Tensile and Impact Bending Tests

Natalia Narkevich [1,*][iD], Ilya Vlasov [1], Mikhail Volochaev [2], Yulia Gomorova [1], Yury Mironov [3][iD], Sergey Panin [4][iD], Filippo Berto [5], Pavel Maksimov [1] and Evgeny Deryugin [1]

[1] Laboratory of Physical Mesomechanics of Materials and Non-Destructive Testing, Institute of Strength Physics and Materials Science SB RAS, 634055 Tomsk, Russia

[2] Kirensky Institute of Physics SB RAS, 660036 Krasnoyarsk, Russia

[3] Laboratory of Shape Memory Alloys, Institute of Strength Physics and Materials Science SB RAS, 634055 Tomsk, Russia

[4] School of Advanced Manufacturing Technologies, National Research Tomsk Polytechnic University, 634030 Tomsk, Russia

[5] Department of Mechanical and Aerospace Engineering, SAPIENZA-Università Di Roma, 00184 Roma, Italy

[*] Correspondence: natnark@list.ru; Tel.: +7-3822-286-827

Abstract: The paper presents the results of tensile and impact bending tests of 17%Cr-19%Mn-0.53%N high-nitrogen austenitic stainless steel in temperatures ranging from -196 to 20 °C. The steel microstructure and fracture surfaces were investigated using transmission and scanning electron microscopes, as well as X-ray diffraction analysis. The steel experiences a ductile-to-brittle transition (DBT); however, it possessed high tensile and impact strength characteristics, as well as the ductile fracture behavior at temperatures down to -114 °C. The correspondence between γ–ε microstructure and fracture surface morphologies was revealed after the tensile test at the temperature of -196 °C. In this case, the transgranular brittle and layered fracture surface was induced by ε-martensite formation. Under the impact bending test at -196 °C, the brittle intergranular fracture occurred at the elastic deflection stage without significant plastic strains, which preceded a failure due to the high internal stresses localized at the boundaries of the austenite grains. The stresses were induced by: (i) segregation of nitrogen atoms at the grain boundaries and in the near-boundary regions, (ii) quenching stresses, and (iii) reducing *fcc* lattice volume with the test temperature decrease and incorporation of nitrogen atoms into *fcc* austenite lattice. Anisotropy of residual stresses was revealed. This was manifested in the localization of elastic deformations of the *fcc* lattice and, consequently, the stress localization in <100>-oriented grains; this is suggested to be the reason of brittle cleavage fracture.

Keywords: high-nitrogen steel; austenite; tensile test; impact bending test; ductile-to-brittle transition; internal stresses; fracture

1. Introduction

A combination of high strength, ductility, formability, resistance to corrosion [1–4] and wear (due to a low friction coefficient [5]), as well as aesthetics and a low cost, promote the use of high-nitrogen steels as an alternative to Cr-Ni steels, in particular, it concerns manufacturing of building constructions. The nickel-free austenitic grades are applied in offshore platforms and various facilities for extraction, transportation and storage of liquefied natural gas at low temperatures [6]. A disadvantage of high-nitrogen steels is a pronounced ductile-brittle transition (DBT) characteristic under tensile and impact bending loads at low temperatures [7–16]. The reasons for DBT are: (i) strong thermally activated nitrogen hardening of a solid solution that increases the normal stresses in the Charpy impact tests, and (ii) the decrease in the mobility of dislocations at low temperatures due to their interaction with dissolved nitrogen atoms at sliding [7]. This can be concluded

from studies [7,8], where any phase transformations are suggested to be suppressed under low-temperature loading. In addition, a rise in DBT temperature (DBTT) was predicted when nitrogen content increased [7]. Additional alloying with copper improved efficiently the impact toughness of Cr-Mn-N steels [8]. With enhancing Mn and Ni contents, both ductility and impact toughness increased at low temperatures, while the DBTT levels decreased [9,11]. Both C and N alloyed steels are characterized by lower DBTT values than those doped with nitrogen alone because of enhancement of the metallic nature of interatomic bonds [12,13].

The DBTT level depends on the austenite stability, which is greater in metastable steels [12]. It was established that most of the brittle fracture regions are parallel to one of the {111} planes in stable austenitic steels. This is associated with the slipping-off phenomenon due to separation occurring along the active slip planes with a high density of dislocations [10,11]. The transgranular brittle fracture of 18%Mn-18%Cr high-nitrogen austenitic steel under the impact bending tests was characterized as "atypical" [10]. Sliding along the active slip planes with a high dislocation density was the cause of the brittle cleavage fracture due to a short-range ordering (SRO) of nitrogen [7]. In the tensile tests at $-196\ ^\circ$C, the fracture behavior of 18%Mn-18%Cr-0.5%N steel greatly depends on a strain rate [14]. It varied from a predominantly brittle type at $2.7\ 10^{-3}$ mm/s to a ductile type at $2.7\ 10^{-1}$ mm/s. The change in the fracture pattern was explained [14] as a transition from the sliding along the active slip planes with a high dislocation density to a rapid motion of massive dislocations within the narrow slip bands. The analysis of DBT nature for high-nitrogen steels at low temperatures indicated the contradiction of this conclusion. The DBT phenomenon does not take place in *fcc* alloys, while the reason for this transition is still unclear for high-nitrogen steels. In papers [2,7], the DBT process is associated with the decrease in the mobility of dislocations during interaction of the latter with nitrogen atoms; however, this phenomenon points out at a strong planar glide of dislocations [10,14]. In addition, the dislocation mobility decreases with increasing the strain rates [15,16]; however, this fact contradicts the data reported in [14]. Therefore, there is a certain scientific knowledge gap that needs to be investigated and filled.

This paper addresses the study of deformation and fracture behavior of Cr-Mn-N high-nitrogen austenitic steel with a stable austenitic microstructure under the tensile and impact bending tests (at negligible and great strain rates, respectively) at low temperatures; the second priority is the DBT nature clarification.

2. Materials and Methods

Cr-Mn-N high-nitrogen steel (Table 1) was melted in a laboratory induction furnace. Then, the steel was cast into sand dies with dimensions of $200 \times 200 \times 50$ mm^3. After removing the top layer, the steel ingots were homogenized at 1250 $^\circ$C for three hours and forged to fabricate plates. Then, the plates were sliced into pieces with dimensions of $100 \times 20 \times 10$ mm^3 by the electrospark method. The subsequent solution treatment was carried out at 1100 $^\circ$C for one hour in order to dissolve any secondary phase precipitates, followed by water quenching.

Table 1. Chemical composition of Cr-Mn-N steel.

Element	Cr	Mn	Si	Ni	C	N	P	S	Fe
Weight, %	16.50	18.81	0.52	0.24	0.07	0.53	0.01	0.001	Bal.

The samples for tensile tests were cut by electrical discharge machining (EDM), mechanically ground, and polished with diamond pastes. Their gauge length was 15 mm, while the cross-sections were 1.0×2.5 mm^2. Before the tests, the samples were electropolished in "H$_3$PO$_4$ (430 mL) + CrO$_3$ (50 g)" electrolyte. Standard Charpy-V notch samples of 10 mm $\times$ 5 mm cross-section and length 55 mm were cut out by EDM and mechanically ground.

The tensile tests were carried out using an "INSTRON 5582" testing machine (Instron, Norwood, MA, USA) at a crosshead speed of 0.002 mm/s at temperatures from −196 up to 20 °C. Three samples of each type with a gauge length of 15 mm and a cross-section area of 1.0×2.5 mm^2 were tested at each temperature level. The values of elongation at a break were determined as the arithmetic means of all three measured levels. Values of a plastic strain work of the samples were determined as the area under stress–strain (σ–ε) curves minus the part corresponded to the elastic ones.

The Charpy impact tests were conducted using an "INSTRON 450MPX" motorized pendulum impact testing system (Instron Corporation, Groove City, PA, USA) according to ASTME 23:2007 at temperatures from −196 up to 20 °C at a load rate of 59.4 m/s.

The fine microstructure of the steel was investigated using a "HT-7700" transmission electron microscope (Hitachi, Tokyo, Japan) at an accelerating voltage of 120 kV. An "FB-2100" focused ion beam system (Hitachi, Tokyo, Japan) was utilized for preparing the cross-section foils.

In addition, the microstructure and phase composition were studied by the X-ray diffraction (XRD) method with the use of a "DRON-7" diffractometer (Bourevestnik JSC, St. Peterburg, Russia) in Co-K$_\alpha$ radiation at room temperature. After the tensile tests, the X-ray diffraction analysis was performed to examine the fracture surfaces without their rotation, while they were rotated after the impact bending tests. The key structural parameters, i.e., dimensions of the coherent scattering regions and <ε> microstrains were determined by Williamson-Hall method [17].

The fracture surfaces were examined with a "LEO EVO 50" scanning electron microscope (Carl Zeiss, Oberkochen, Germany). An accelerating voltage was 20 kV. The regions at the specimen center, as well as on the ones located at 1, 4 and 7 mm below the notch, were observed.

3. Results

3.1. The Tensile Tests

3.1.1. Temperature Dependences of a Strain

Figure 1 shows the engineering stress–strain (σ–ε) curves for Cr-Mn-N steel, determined under the tensile tests at various temperatures. In all investigated cases, including a cryogenic temperature of −196 °C, the steel exhibited continuous yielding.
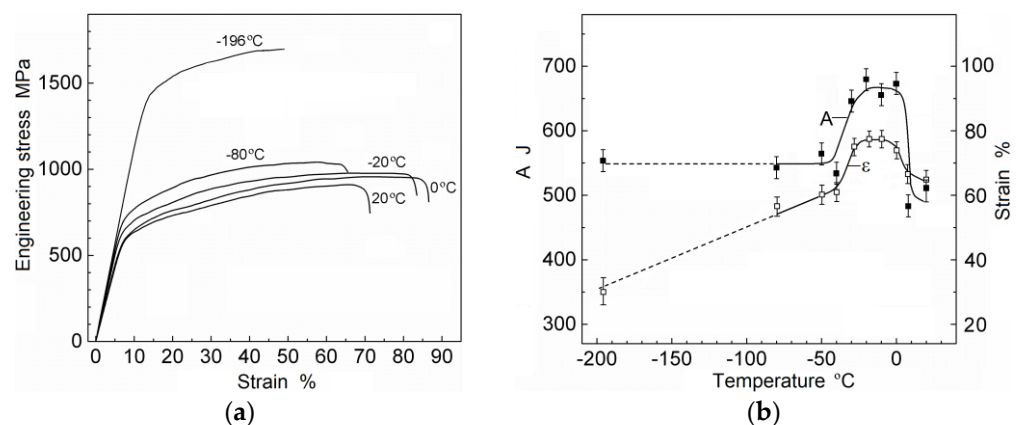

Figure 1. The engineering (σ–ε) tensile curves for Cr-Mn-N steel at various testing temperatures (**a**); the temperature dependences of the strain and work of a plastic strain (**b**).

Both the yield point ($\sigma_{0.2}$) and the ultimate tensile strength (σ_{uts}) increased with lowering temperatures. When it decreased from 20 to −80 °C, the σ_{uts} values increased from 850 up to 1000 MPa, while the σ_{uts} rose more significantly in the temperature range of −80−−196 °C, reaching the level of 1700 MPa. The non-linear dependence of the σ_{uts} versus the test temperature meant different both the strain and the hardening mechanisms in these two ranges.

The strain localization and neck formation preceded the failure of all samples tested in the temperature range from −80 to 20 °C. At the cryogenic temperature of −196 °C, the sample fractured with an instantaneous load drop excluded the strain localization stage (Figure 1a). The temperature dependences of the plastic stain work (Figure 1b) mostly correlated with the described pattern of the ductility changing dynamics. The exception was the cryogenic temperature of −196 °C, at which the plastic stain work value was greater than that at room temperature due to the high ductility (30%) and ultimate tensile strength (1700 MPa). The non-monotonic (with pronounced maximum) pattern of the ductility variation was observed in [18–20]; it was shown that high values of elongation at break were caused by deformation twinning as well as ε-martensite formation.

3.1.2. Microstructural Studies

Figure 2 presents the microstructure of the studied steel after the tensile test at −196 °C. One can easily see the deformation twins up to 50 nm wide and ε-martensite with *hcp* lattice.
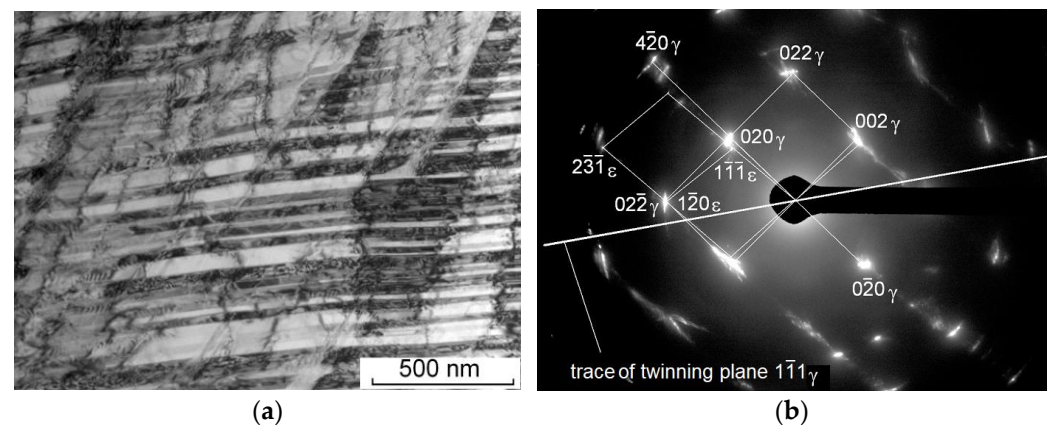

(**a**)   (**b**)

Figure 2. The microstructure of Cr-Mn-N steel after the tensile test at $T = -196$ °C (**a**) and the electron diffraction pattern of γ-phase (z = $[100]_\gamma$ and z = $[120]_\gamma$) as well as ε-martensite z = $[211]\varepsilon$ (**b**).

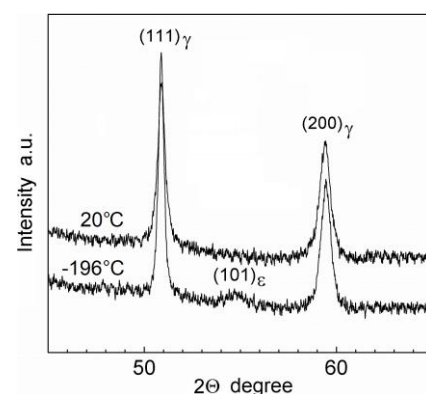The reflection from $(101)_\varepsilon$ plane was also observed in the corresponding diffraction pattern (Figure 3).

Figure 3. Fragments of XRD diffraction patterns of Cr-Mn-N steel after the tensile tests at $T = 20$ °C and $T = -196$ °C.

The ε-martensite with *hcp* lattice was formed upon the Cr-Mn-N steel deformation due to its low stacking fault energy (SFE) of ~20 mJ/m^2. A high probability of its nucleation was suggested in [21–23]. In the low-temperature tensile tests, a stress relaxation occurs due to $\gamma \rightarrow \varepsilon$ transformation at the interface between *fcc* austenite lattice and stacking faults. The transformation was a mechanism that promoted the increase in the steel ductility.

Nonuniform nucleation of the ε-martensite crystals could also develop at the boundaries of the deformation twins, which were monolayers with *hcp* lattice. Since twinning was the main deformation mechanism for the steels with SFE $\geq$ 20 mJ/m^2 [23], consequently, the concentration increase in the twin boundaries when enhancing the deformation degree and/or decreasing the test temperature resulted in $\gamma{\rightarrow}\varepsilon$ transformation. Hence, the layered γ–ε microstructure was formed, in which the phases with different crystal lattices were separated by the twin boundaries deformation, as shown in Figure 4. The high values of the stain and work of a plastic strain of the samples, which possessed their maximum in the temperature range from -30 up to 0 $^{\circ}$C (Figure 1b), were caused by the transformation of *fcc* lattice into *hcp* lattice.
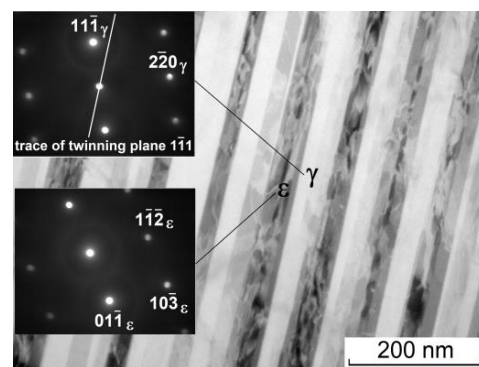

Figure 4. A bright-field TEM-micrograph of the Cr-Mn-N steel fine structure after the tensile test at -196 $^{\circ}$C and the electron nanodiffraction patterns of the ε-martensite (z = [311]) and austenite (z = [112]$_{\gamma}$) plates.

The austenite possesses a lower elastic modulus than that of ε-martensite. After the formation of the deformation-induced crystals with *hcp* lattice, the strain was localized in the ε-martensite plates during the tensile tests. This caused their fracture, ensuring a failure of the samples then. The lower the test temperature was, the less strain level was necessary for running $\gamma{\rightarrow}\varepsilon$ transformation and subsequent fracture of the ε-martensite plates.

3.1.3. Fractographic Investigations

The fracture surfaces of the samples are shown in Figure 5. In the temperature range from $T = -80$ to $T = 20$ $^{\circ}$C, they were characterized mostly by a ductile pattern. The morphology was represented by the dimples with smoothed flat foundations. Figure 5a,b indicate the development of the shear deformation upon the failure. The fracture pattern was predominantly brittle transgranular one, the morphological features of which was represented by laminations (at a tensile test temperature of -196 $^{\circ}$C). Such patterns of the fracture surfaces were a reflection of a double-phase γ–ε microstructure of the sample, in which the failure occurred along the ε-martensite plates with *hcp* lattice.

(a) (b) (c)
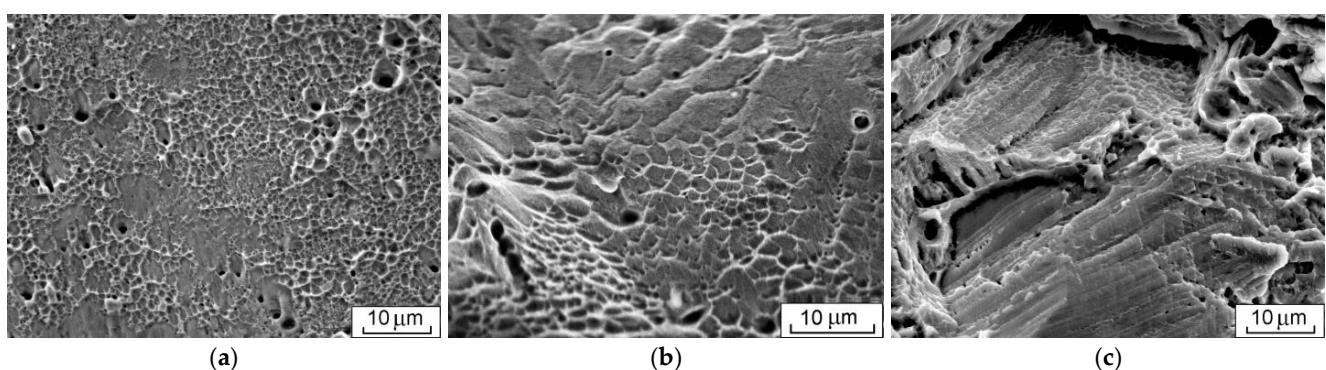
Figure 5. The fracture surfaces of the samples after the tensile tests at $T = -30$ $^{\circ}$C (**a**), $T = -80$ $^{\circ}$C (**b**) and $T = -196$ $^{\circ}$C (**c**).

3.2. The Charpy Impact Tests

3.2.1. Temperature Dependences on Impact Toughness

Figure 6 shows the impact loading diagrams for the Charpy-*V* specimens tested at various temperatures. They were characterized by several stages. Stage *I* corresponded to the elastic bending of the specimens and was evidenced by a linear dependence of load (*F*) vs. deflection (*S*). The tangent of the slope of the linear section to the abscissa axis did not depend on a test temperature (tg α = 16.5 kN/mm). At stage *II*, the load increased up to its maximum value (F_{max}). As a result, the specimens were plastically deformed, the load enhanced up to an extremely great value (with the strain localization in the vicinity of the notch), where some microcracks appeared. The oscillating pattern of the curves from point F_y to F_{max} characterized the discrete deformation process, as well as the nucleation and propagation of microcracks, which transform into the main crack at point F_{max}. The main crack growth occurred at stage *III*. In this case, the slope of the curve of the impact loading diagrams to the abscissa axis increased with the temperature fall, i.e., the propagation rate of the main crack enhanced. At $T = -196$ °C, the specimens fractured in a brittle way at an infinitely high rate (Figure 6c). In this diagram, only stage *I* was observed, and the maximum load (F_{max}) corresponded to the onset of brittle fracture (F_{bf}); the plastic deformation stage was bypassed.
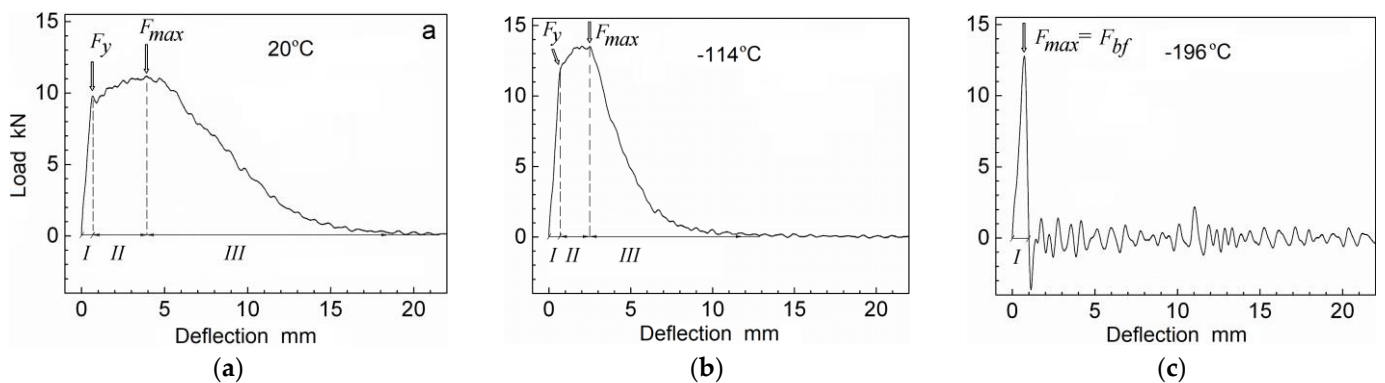

Figure 6. The impact loading diagrams for the Charpy-V specimens tested at $T = 20$ °C (**a**), $T = -114$ °C (**b**) and $T = -196$ °C (**c**).

Figure 7 presents a scheme for determining the external load work at all stages of the impact bending tests and its temperature dependences at stages *II* and *III* (designated as A_{II} and A_{III}). The area under the rising portion of the impact loading diagram A_{II} characterized the work, associated with the plastic strains and the appearance of the main crack [24]. The area under the descending portion of the diagram A_{III} reflected a part of the work responsible for the main crack propagation. Analysis of Figure 7 made it possible to suggest that A_{III} value was greater than value A_{II} in the studied temperature range, except for the cryogenic level of -196 °C, at which the specimen fractured immediately after the elastic bending (in this case, $A_{II} = A_{III} = 0$). When the test temperature was reduced from $T = 20$ to $T = -100$ °C, both A_{II} and A_{III} values synchronously decreased. A sharp lowering of KCV on A_{III} level began at temperatures below -100 °C, reaching its minimum 15 J/cm^2 at $T = -196$ °C (Figure 8).

3.2.2. Fractographic Investigations

After the impact bending tests, the fracture surfaces were analyzed in the three zones which characterize the main crack propagation stages: in the vicinity of the notch (A), in the specimen center (B), and at the fracture region (C), according to Figure 9.
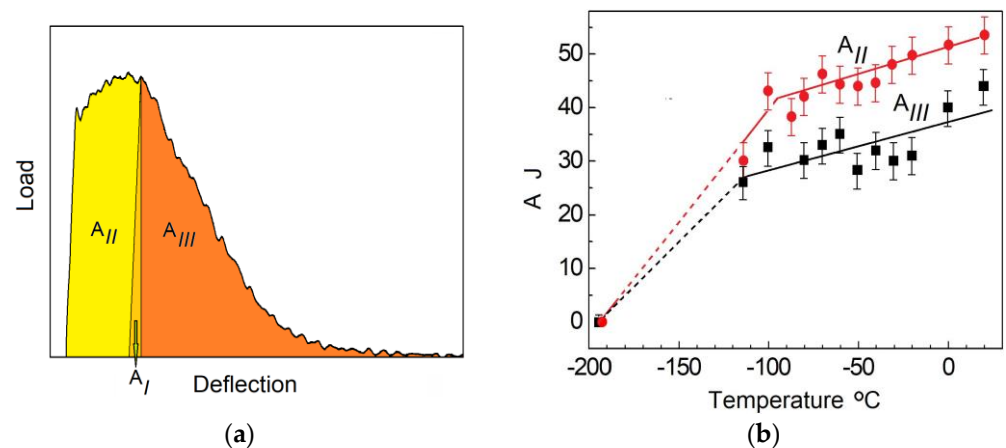
(**a**)　　　　　　　　　　　　　　　　(**b**)

Figure 7. The scheme for external load work at all deformation and fracture stages during the impact bending tests (**a**), where A_I is the work associated with the elastic strains, A_{II}–with the plastic stains and the main crack appearance, and A_{III}–with the main crack propagation; A_{II} and A_{III} temperature dependences (**b**).
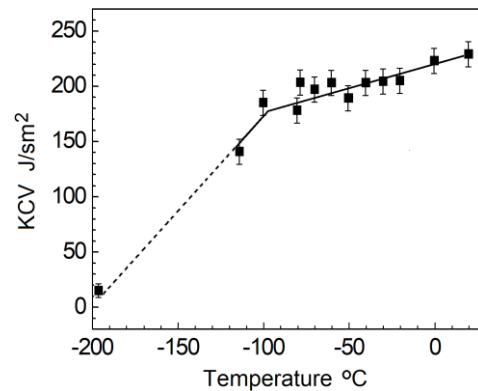

Figure 8. The KCV versus test temperature dependence for Cr-Mn-N steel.

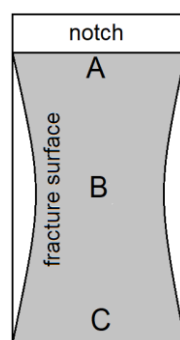**Figure 9.** The fracture surface scheme, where A, B, and C are the sites of the observation zones.

At the temperatures fall up to $T = -114\,°C$, the ductile fracture with formation of large (up to 50 µm) and small (about 1 µm) dimples was evident; we could not reveal any signs of a brittle fracture in all zones (Figure 10). The elongated dimples, being characteristic of the shear strain, were evident at all stages of crack's development, see zones A, B, and C. However, the specimen failure was predominantly brittle at $T = -196\,°C$. In this case, the dimple fragments occupied less than 3% of the total fracture surface area. Note that the fracture surface morphology in the form of a brittle intergranular cleavage (Figure 10) after the impact bending tests differed from the brittle transgranular type after the tensile tests (Figure 5).
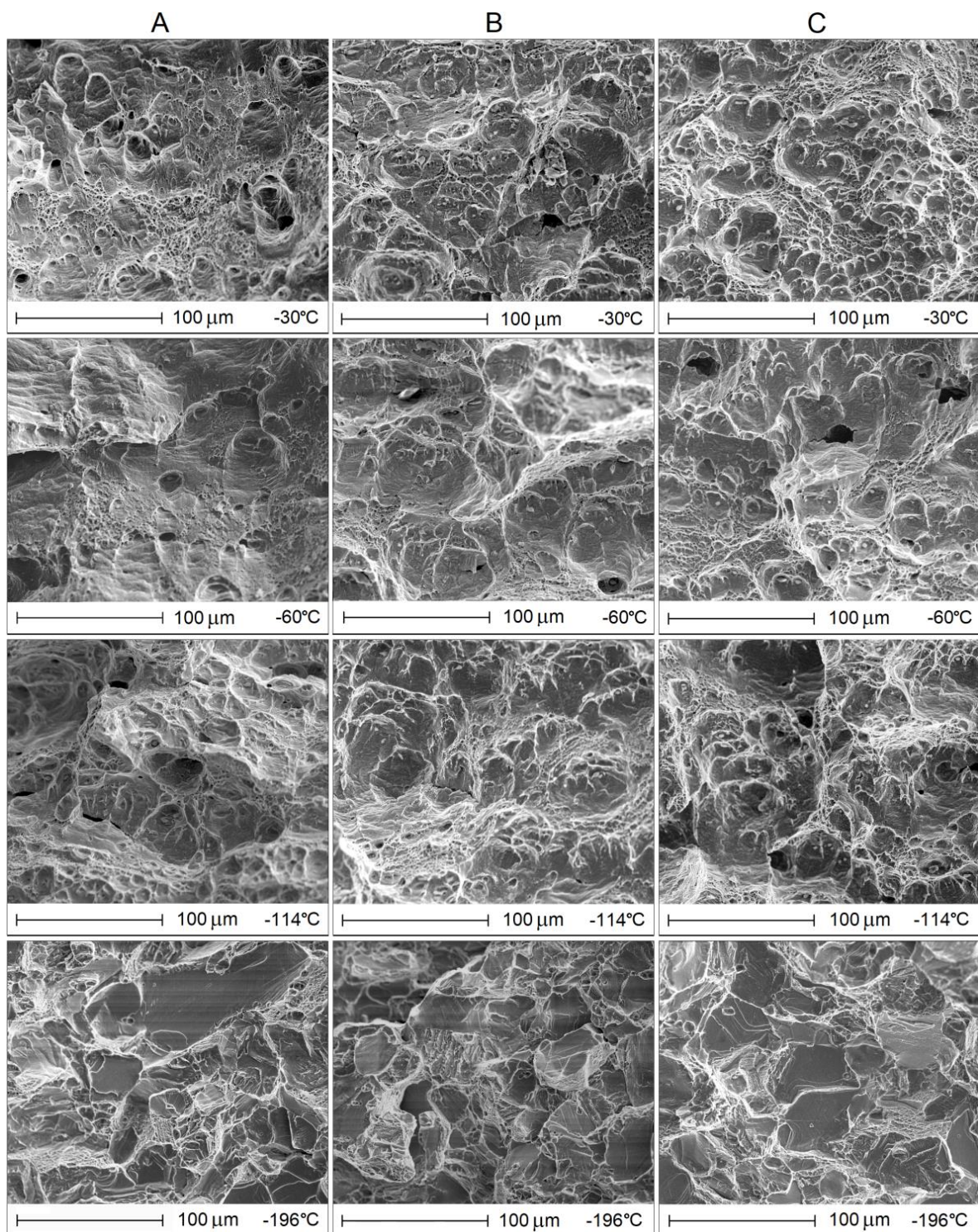
Figure 10. The fracture surfaces of the Charpy specimens after the impact bending tests at $T = -30$ °C, $T = -60$ °C, $T = -114$ °C, and $T = -196$ °C (**A**–**C**).

At the low tensile strain rate, the characteristic layering was observed (Figure 5). However, smooth fragments of the fracture surface, equal in their sizes to the grains, were found after impact loading (Figure 10). Some of them possessed a line-like morphology, being oriented at the angle of 60°, while others were completely smooth. This pattern was traced at all stages of the main crack propagation, in all zones A, B and C, according to Figure 9.

3.2.3. X-Ray Diffraction

After the impact bending test at $T = -196\,^{\circ}\text{C}$, the fracture surface of the Charpy-V specimen was examined by X-ray diffraction. The results showed the presence of the only austenitic phase, similar to how it was before the test (Figure 11a). Figure 11b presents linear dependences y_1 for the planes (111), (220), (311), (222) and y_2 for the planes (200)–(400), in which $a = 0$ (within the range of a measurement error). Consequently, the contribution of the refinement of coherent scattering regions (CSRs) to the physical broadening of reflections was insignificant and did not depend on the crystallographic direction. This fact meant that the key factor determining the broadening of the reflections was the magnitude of $<\varepsilon>$ microstrains of *fcc* lattice, which depended substantially on the crystallographic direction. A level of the elastic microstrains $<\varepsilon>$ in the [111]-oriented grains was 0.0015 in the direction perpendicular to the fracture surface. The value was much lower than that in the [200]-oriented ones of 0.0036. Young's modulus E_{hkl} values were determined in [25] as $E_{111} = 256.1$ GPa and $E_{200} = 161.7$ GPa. Thus, the stress levels were $\sigma = 384$ and $\sigma = 582$ MPa in the [111] soft- and the [200] hard-oriented grains, respectively.
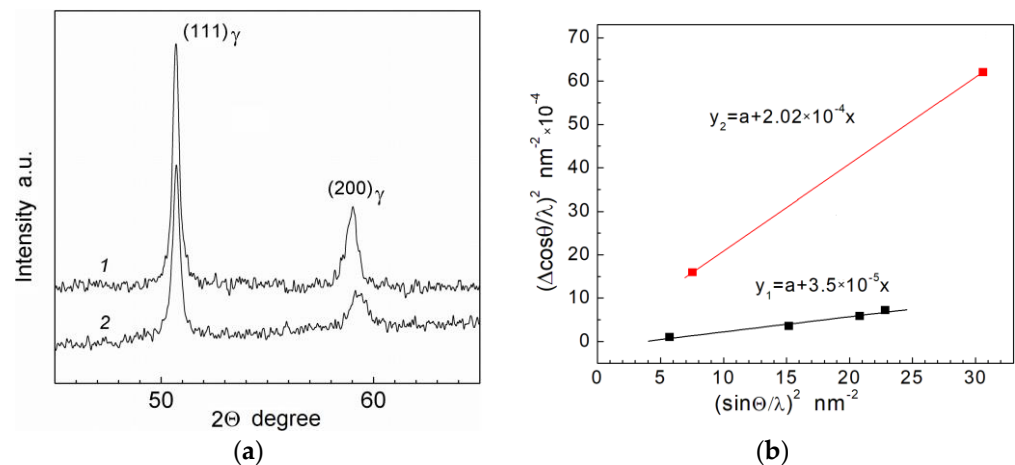

(**a**)　　　　　　　　　　　　　　　(**b**)

Figure 11. Fragments of the diffraction patterns of Cr-Mn-N steel before (1) and after (2) the impact bending test at $T = -196\,^{\circ}\text{C}$ (the fracture surface was analyzed in the latter case) (**a**); linear dependences y_1 for the planes (111), (220), (311), (222) and y_2 for the planes (200)–(400), in which $a = 0$ within the range of a measurement error (**b**).

4. Discussion

Differing from both bcc and *hcp* metals and alloys, much less data were reported on the brittle fracture of steels with *fcc* lattice [26]. Most *fcc* metals and steels exhibited the high ductility under different loading conditions and over a wide range of temperatures, including the cryogenic levels. In such materials, dislocations glide easily since "stresses required for cleavage cannot be achieved, because their levels are limited by the "involvement of the slip mechanism" [26]. Interstitially alloyed nickel-free austenitic stainless steels occupied a special place among austenitic grades with *fcc* lattice. In recent years, much attention has been paid to research on their DBT features [7–12,14–16]. Milititsky et al. [8] reported that the strong decrease in their impact toughness with lowering temperature is associated with nitrogen alloying. According to the empirical relationship DBTT = 300[%N]–303[°C] [27], the nitrogen content is the most critical parameter. Nitrogen atoms located at interstices of the crystal lattice are surrounded by Mn and Cr atoms of transition metals (positioned to the left of iron in the periodic table). This phenomenon contributes to the formation of the regions with short-range ordering (SRO). In turn, this provokes a planar slip during deformation, increasing the strain hardening and resistance to a stress localization [8,10,28–31]. Along with this, the root-mean-square (RMS) displacements of atoms from their equilibrium positions occur in *fcc* quenched steels. In the <100> direction, the RMS was 0.0042 nm, but it was not observed in the <111> direction [32]. The

presence of SRO and the RMS indicate a highly non-equilibrium state of a solid solution, in which nitrogen occupied interstitial positions.

The non-equilibrium state of *fcc* lattice is enhanced at low and cryogenic temperatures, while the probability of the stacking fault formation increases. Low-temperature deformation stimulates $\gamma \rightarrow \varepsilon$-transformation at the boundaries of the deformation twins. The ε-martensite formation with *hcp* lattice is induced by the compressive stresses, since *hcp* lattice has a smaller volume than *fcc* lattice in the high-nitrogen steels [21]. The decrease in the volume of *fcc* lattice occurs when the steel is cooled down before testing due to its thermal compression; the lower the temperature, the greater the decrease. Under the low-temperature tensile testing, the compression strains increase locally, which is the driving force of $\gamma \rightarrow \varepsilon$ transformation.

Lee et al. [33,34] as well as Wang et al. [35] reported the patterns of the strained structure as a function of nitrogen content. Nitrogen stabilizes austenite, so increasing its content in the range of 0.3–1.0 wt.% contributing to the twinning-dominant deformation of Cr-Mn-N steels. Indeed, a cross-slip of dislocations is suppressed in the austenitic steels with SFE levels of above 20–25 mJ/m^2. However, such steels possessed high ductility and strain hardening in the tensile tests at room temperature and of particular at low ones. Deformation twinning and the $\gamma \rightarrow \varepsilon$ transformation mechanisms were predominant at low test temperatures and the strain rates [18]. Therefore, the current study shows that the ductility of Cr-Mn-N steel was 30% at −196 °C, which confirmed its great ability to relax external loads (Figure 1). The combination of the high ductility and brittle fracture reflected the fact that the steel became brittle during deformation by changing its phase composition.

Liu, S. et al. [36] reported that the transgranular fracture initiated by the microcracks formed at intersections of the strained microstructure. Such microcracks propagate towards the adjacent cracks on different {111} planes, forming the transgranular fracture facets with steps and river patterns. At the same time, Figure 4 clearly shows that the formation of the transgranular brittle fracture pattern could develop along the ε-martensite plates parallel to the {111} planes of austenite, providing that the {111}$_\gamma$ ||{001}$_\varepsilon$ orientation relation is kept.

In the impact bending tests at the high load rate, $\gamma \rightarrow \varepsilon$ transformation did not take place. In the temperature range from $T = -114$ to $T = 20$ °C the steel was fractured in a ductile way. The predominantly brittle cleavage fracture pattern was observed at $T = -196$ °C. Vologzhanina et al. [37] showed that the high deformation rates prevented or completely suppressed the phase transformations in steels, which was confirmed in the current study.

Under the impact bending tests at $T = -196$ °C, the brittle intergranular fracture indicated that the steel specimens failed without pronounced plastic strains at the stress levels less than that required for a plastic shear under such conditions (Figure 6c). At the given test temperature, the ductile or brittle failure pattern depended on what was achieved initially: the yield point or the fracture stress value [27]. In the case of high internal stresses due to alloying with nitrogen, the fracture stress at $T = -196$ °C was reached first.

At the cryogenic temperature and the high load rate, among the factors that blocked the plastic strains in *fcc* lattice, there was a segregation effect in the form of a gradient of nitrogen, chromium, and manganese concentrations in the austenite grains as well as at their boundaries [27,38]. The increased contents of the alloying elements (nitrogen, of particular) at the boundaries and in the near-boundary zones caused the local increase in the parameter and volume of *fcc* lattice in these regions. Consequently, the internal stresses in the near-boundary regions were higher compared to the bulk of the grains, and they further increased with a temperature decrease.

Another factor in the non-equilibrium structure was the formation of the residual tensile internal stresses in *fcc* lattice of Cr-Mn-N steel after its quenching (Figure 12). The *fcc* austenite lattice was distorted to the greatest extent along the <100> direction [39], since Young's modulus E_{200} was lower than E_{hkl} for other crystallographic directions [25]. After quenching of Cr-Mn-N steel, its low thermal conductivity λ was a source of the residual stresses; the values of the former were 24 and 10 W/m·K at 800 °C and 20 °C, respectively.

Taking into account the concentration gradient of the alloying elements (especially nitrogen) at the boundaries of the austenite grains as well as inside them, the localization of the hardening stresses in the boundary zones could be assumed.
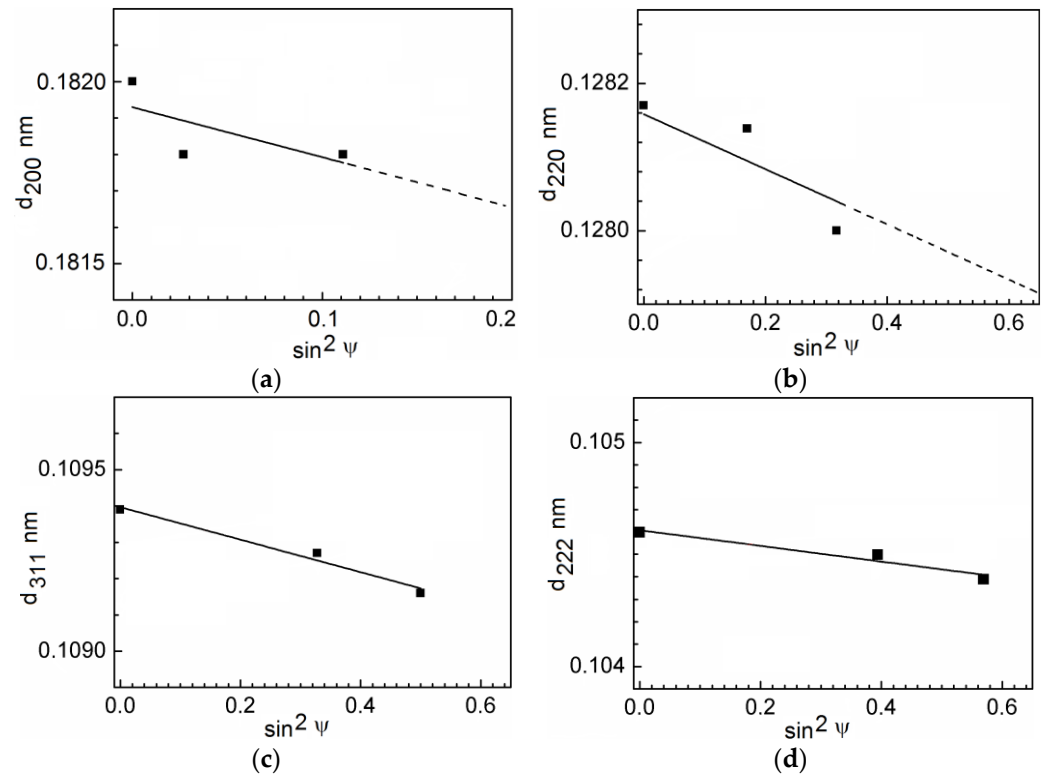

Figure 12. Lattice distances d200 (**a**), d220 (**b**), d311 (**c**), and 222 (**d**) of the Cr-Mn-N steel after its quenching as functions of $\sin^2\psi$ (Co-Kα radiation) [39].

It was of interest to compare the obtained results with those for Hadfild steel, which possesses the same thermal conductivity [40]. Its heating up to $T = 1100$ °C followed by quenching in water is used to dissolve the secondary phases (carbides) and form the single-phase austenite microstructure. After quenching, both the Hadfield and high-nitrogen steels fail in a brittle way under impact loads at temperatures below -100 °C. At the same time, the interstitial impurities were almost absent in Cr-Ni and Cr-Ni-Mo steels. During the heat treatment, there was no sense that achieving such high temperatures and the steels' thermal conductivity λ of 36 W/m K at $T = 800$ °C was greater compared to that for the high-nitrogen steels. As a result, no low-temperature brittleness was revealed [3,7,35,41].

The reason for the pronounced DBT in the high-nitrogen steels was a sum of factors. However, the stress state formed prior to low-temperature testing among them has not been so far. Meanwhile, it was known that alloying with nitrogen increased the lattice parameter of austenite. As the temperature decreased, the lattice parameter and its volume reduced, and the nitrogen concentration became super-equilibrium. This contributed to an increase in the internal stresses to a critical value, especially at the grain boundaries, where the nitrogen concentration was enhanced.

A strong orientational dependence of the elastic modulus is characteristic of high-nitrogen steels [25]. The former governs the anisotropy of both (i) internal stresses during cooling down to cryogenic temperature and (ii) residual stresses after the mechanical testing. It was shown that after low-temperature tests, residual stresses were predominantly localized in [200] oriented grain. The value of residual stresses was much lower in grains with a different crystallographic orientation. These shed light on the steel fracture mechanisms at the stage of elastic deflection under the temperature of -196 °C. In particular, the fracture stress was achieved in [200] orientated grains at lower strains in contrast with

differently oriented crystallites. The cleavage and quasi-cleavage fracture pattern indicated the "selectivity" of the main crack propagation path, namely, it was oriented along grains with an unfavorable crystallographic orientation.

Therefore, the relaxation of stresses occurred by breaking the interatomic bonds due to the high strain rate in the impact bending tests at $T = -196\,°C$ under reduced dislocation mobility conditions when $\gamma \rightarrow \varepsilon$ transformation do not develop. The cleavage failure started predominantly from the grain boundaries, since the internal stresses were localized precisely there. The authors believe that the issue of the predominance of the close-packed {111} cleavage planes is still debatable and this makes the research field relevant to study further.

5. Conclusions

The temperature dependences of the mechanical properties and the fracture behavior of Cr-Mn-N steel were investigated by the tensile and impact bending tests in the temperature range from -196 to $20\,°C$. As a result, the following conclusions were drawn.

1. Cr-Mn-N steel demonstrated a high ductility in the tensile tests at the constant load rate of 0.002 mm/s over the entire temperature range with a change in the fracture behavior from a ductile at $T = -80$–$20\,°C$ to a brittle transgranular at $T = -196\,°C$. At the cryogenic level, the ductility of 30% was achieved due to the development of $\gamma \rightarrow \varepsilon$ transformation, while ε-martensite provoked a brittle fracture;
2. In the impact bending tests under the load rate of 59.4 m/s, the fracture pattern changed from ductile in the temperature range from -114 up to $20\,°C$ to brittle intergranular one (predominantly by cleavage) at $T = -196\,°C$. This failure type was characteristic to the absence of $\gamma \rightarrow \varepsilon$ transformation;
3. The analysis of the impact loading diagrams showed that the plastic strain work related to the nucleation and propagation of the main crack from the Charpy notch decreased with lowering the test temperature from $T = 20$ down to $-114\,°C$. At $T = -196\,°C$, the failure occurred immediately after the end of the elastic deflection stage. The external load work associated with the crack propagation sharply reduced at the temperatures below $-100\,°C$, reaching the zero level at $T = -196\,°C$;
4. A possible reason for the DBT process in the high-nitrogen steel at low temperatures was great stresses formed due to: (i) enrichment of near-boundary zones with nitrogen, chromium, and manganese; (ii) a low thermal conductivity, which contributed to the formation of the quenching stresses, and (iii) a decrease in the volume of *fcc* lattice with lowering the test temperature. At $T = 20\,°C$, the equilibrium content of nitrogen, forming an interstitial solid solution, transformed to the super-equilibrium one at $T = -196\,°C$. In this case, the stresses reached the critical values, the relaxation of which could take place only by breaking the interatomic bonds without a significant effect of the dislocation mechanisms due to the plastic strains.

Author Contributions: Conceptualization, N.N.; validation, N.N.; writing—original draft preparation, N.N.; writing—review and editing, N.N., S.P. and F.B.; investigation, I.V., M.V., Y.G. and Y.M.; visualization, P.M.; funding acquisition, E.D. All authors have read and agreed to the published version of the manuscript.

Data Availability Statement: Not applicable.

Conflicts of Interest: The authors declare no conflict of interest.

References

1. Gavriliuk, V.G.; Berns, H. *High Nitrogen Steels: Structure, Properties, Manufacture, Applications*; Springer: Berlin, Germany, 1999; p. 135.
2. Nordberg, H.; Bjorklund, J. *Application of Stainless Steels*; Avesta Research Foundation: Stockholm, Sweden, 1992; pp. 62–71.
3. Katada, Y.; Sagara, M.; Kobayashi, Y.; Kodama, T. Fabrication of High Strength High Nitrogen Stainless Steel with Excellent Corrosion Resistance and Its Mechanical Properties. *Mater. Manuf. Process.* **2004**, *19*, 19–30. [CrossRef]
4. Narkevich, N.A.; Deryugin, E.E.; Perevalova, O.B.; Vlasov, I.V. Effect of Ultrasonic Forging Strain Processing on the Surface Layer Microstructure and Temperature-Dependent Mechanical Properties of High Nitrogen Austenitic Steel. *Mater. Sci. Eng. A* **2022**, *834*, 142590. [CrossRef]
5. Korshunov, L.G.; Goikhenberg, Y.N.; Tereshchenko, N.A.; Uvarov, A.I.; Makarov, A.V.; Chernenko, N.L. Wear Resistance and Surface Structure of Nitrogen-Containing Stainless Austenitic Steels upon Friction and Abrasive Wear. *Phys. Met. Metallogr.* **1997**, *84*, 554–561.
6. Layus, P.; Kah, P.; Martikainen, J.; Pirinen, M.; Khlushova, E.; Ilyin, A. European and Russian Metals for Arctic Offshore Structures. In Proceedings of the International Offshore and Polar Engineering Conference, Anchorage, AK, USA, 30 June–5 July 2013.
7. Tanaka, M.; Onomoto, T.; Tsuchiyama, T.; Higashida, K. Brittle-to-Ductile Transition in Nickel-Free Austenitic Stainless Steels with High Nitrogen. *ISIJ Int.* **2012**, *52*, 915–921. [CrossRef]
8. Mililtsky, M.; Matlock, D.K.; Regully, A.; Dewispelaere, N.; Penning, J.; Hanninen, H. Impact toughness properties of nickel-free austenic stainless steels. *Mater. Sci. Eng. A* **2008**, *496*, 189–199. [CrossRef]
9. Xu, M.; Wang, J.; Liu, C. Low Temperature Deformation Behavior of High-Nitrogen Nickel-Free Austenitic Stainless Steels. *Jinshu Xuebao/Acta Metall. Sin.* **2011**, *47*, 1335–1341. [CrossRef]
10. Tomota, Y.; Xia, Y.; Inoue, K. Mechanism of Low Temperature Brittle Fracture in High Nitrogen Bearing Austenitic Steels. *Acta Mater.* **1998**, *46*, 1577–1587. [CrossRef]
11. Hwang, B.; Lee, T.H.; Park, S.J.; Oh, C.S.; Kim, S.J. Ductile-to-Brittle Transition Behavior of High-Nitrogen 18Cr-10Mn-0.35N Austenitic Steels Containing Ni and Cu. *Mater. Sci. Forum* **2010**, *654*, 158–161. [CrossRef]
12. Hwang, B.; Lee, T.H.; Kim, S.J. Effect of Alloying Elements on Ductile-to-Brittle Transition Behavior of High-Interstitial-Alloyed 18Cr-10Mn Austenitic Steels. *Procedia Eng.* **2011**, *10*, 409–414. [CrossRef]
13. Tian, K.V.; Passaretti, F.; Nespoli, A.; Placidi, E.; Condò, R.; Andreani, C.; Licoccia, S.; Chass, G.A.; Senesi, R.; Cozza, P. Composition—Nanostructure steered performance predictions in steel wires. *Nanomaterials* **2019**, *9*, 1119. [CrossRef]
14. Tomota, Y.; Nakano, J.; Xia, Y.; Inoue, K. Unusual Strain Rate Dependence of Low Temperature Fracture Behavior in High Nitrogen Bearing Austenitic Steels. *Acta Mater.* **1998**, *46*, 3099–3108. [CrossRef]
15. Sun, G.; Zhang, Y.; Sun, S.; Hu, J.; Jiang, Z.; Ji, C.; Lian, J. Plastic Flow Behavior and Its Relationship to Tensile Mechanical Properties of High Nitrogen Nickel-Free Austenitic Stainless Steel. *Mater. Sci. Eng. A* **2016**, *662*, 432–442. [CrossRef]
16. Sun, G.; Yu, A.; Sun, S.; Ji, C.; Jiang, Z.; Lian, J. Plastic Deformation and Fracture Behaviour of High-Nitrogen Nickel-Free Austenitic Stainless Steel. *Mater. Sci. Technol.* **2017**, *33*, 1635–1644. [CrossRef]
17. Williamson, G.K.; Hall, W.H. X-Ray Line Broadening from Filed Aluminium and Wolfram. *Acta Metall.* **1953**, *1*, 22–31. [CrossRef]
18. Narkevich, N.; Deryugin, Y.; Mironov, Y. Effect of the Γ→ε Phase Transition on Transformation-induced Plasticity (Trip) of Nickel-free High Nitrogen Steel at Low Temperatures. *Metals* **2021**, *11*, 710. [CrossRef]
19. Martin, S.; Wolf, S.; Martin, U.; Krüger, L.; Rafaja, D. Deformation Mechanisms in Austenitic TRIP/TWIP Steel as a Function of Temperature. *Metall. Mater. Trans. A Phys. Metall. Mater. Sci.* **2016**, *47*, 49–58. [CrossRef]
20. Wang, W.; Yan, W.; Yang, K.; Shan, Y.; Jiang, Z. Temperature Dependence of Tensile Behaviors of Nitrogen-Alloyed Austenitic Stainless Steels. *J. Mater. Eng. Perform.* **2010**, *19*, 1214–1219. [CrossRef]
21. Sagaradze, V.V.; Kataeva, N.V.; Kabanova, I.G.; Afanasev, S.V.; Pavlenko, A.V. Effect of the Temperature of Shock-Wave Loading on Structure and Phase Transformations in Nitrogen-Containing Austenitic Cr–Mn–Ni Steel. *Phys. Met. Metallogr.* **2020**, *121*, 683–688. [CrossRef]
22. Narkevich, N.A.; Surikova, N.S. Deformation Behavior and Structural Evolution of Stainless Cr–Mn–N Steel during Low-Temperature Tension. *Phys. Met. Metallogr.* **2020**, *121*, 1175–1181. [CrossRef]
23. Lee, T.H.; Shin, E.; Oh, C.S.; Ha, H.Y.; Kim, S.J. Correlation between Stacking Fault Energy and Deformation Microstructure in High-Interstitial-Alloyed Austenitic Steels. *Acta Mater.* **2010**, *58*, 3173–3186. [CrossRef]
24. Panin, S.V.; Maruschak, P.O.; Vlasov, I.V.; Sergeev, V.P.; Ovechkin, B.B.; Neifeld, V.V. Impact Toughness of 12Cr1MoV Steel. Part 2—Influence of High Intensity Ion Beam Irradiation on Energy and Deformation Parameters and Mechanisms of Fracture. *Theor. Appl. Fract. Mech.* **2016**, *83*, 82–92. [CrossRef]
25. Ojima, M.; Adachi, Y.; Tomota, Y.; Ikeda, K.; Kamiyama, T.; Katada, Y. Work Hardening Mechanism in High Nitrogen Austenitic Steel Studied by in Situ Neutron Diffraction and in Situ Electron Backscattering Diffraction. *Mater. Sci. Eng. A* **2009**, *527*, 16–24. [CrossRef]
26. Gandhi, C.; Ashby, M.F. Fracture-Mechanism Maps for Materials which Cleave: F.C.C., B.C.C. and H.C.P. Metals and Ceramics. In *Perspectives in Creep Fracture*; Elsevier: Amsterdam, The Netherlands, 1983. [CrossRef]
27. Hwang, B.; Lee, T.H.; Park, S.J.; Oh, C.S.; Kim, S.J. Correlation of Austenite Stability and Ductile-to-Brittle Transition Behavior of High-Nitrogen 18Cr-10Mn Austenitic Steels. *Mater. Sci. Eng. A* **2011**, *528*, 7257–7266. [CrossRef]

28. Kim, J.M.; Kim, S.J.; Kang, J.H. Effects of Short-Range Ordering and Stacking Fault Energy on Tensile Behavior of Nitrogen-Containing Austenitic Stainless Steels. *Mater. Sci. Eng. A* **2022**, *836*, 142730. [CrossRef]

29. Masumura, T.; Seto, Y.; Tsuchiyama, T.; Kimura, K. Work-Hardening Mechanism in High-Nitrogen Austenitic Stainless Steel. *Mater. Trans.* **2020**, *61*, 678–684. [CrossRef]

30. Kubota, S.; Xia, Y.; Tomota, Y. Work-Hardening Behavior and Evolution of Dislocation-Microstructures in High-Nitrogen Bearing Austenitic Steels. *ISIJ Int.* **1998**, *38*, 474–481. [CrossRef]

31. Simmons, J.W. Overview: High-Nitrogen Alloying of Stainless Steels. *Mater. Sci. Eng. A* **1996**, *207*, 159–169. [CrossRef]

32. Narkevich, N.; Surikova, N.; Vlasov, I.; Narkevich, V.; Deryugin, Y.; Perevalova, O. Effect of Electron-Beam Treatment on the Elemental Composition and Static Displacements of Atoms in the Nearsurface Layer of Cr-Mn-N Austenitic Steel. *AIP Conf. Proc.* **2019**, *2167*, 020238. [CrossRef]

33. Lee, T.H.; Oh, C.S.; Kim, S.J. Effects of Nitrogen on Deformation-Induced Martensitic Transformation in Metastable Austenitic Fe-18Cr-10Mn-N Steels. *Scr. Mater.* **2008**, *58*, 110–113. [CrossRef]

34. Lee, T.H.; Ha, H.Y.; Hwang, B.; Kim, S.J.; Shin, E. Effect of Carbon Fraction on Stacking Fault Energy of Austenitic Stainless Steels. *Metall. Mater. Trans. A* **2012**, *43*, 4455–4459. [CrossRef]

35. Wang, S.; Yang, K.; Shan, Y.; Li, L. Plastic Deformation and Fracture Behaviors of Nitrogen-Alloyed Austenitic Stainless Steels. *Mater. Sci. Eng. A* **2008**, *490*, 95–104. [CrossRef]

36. Liu, S.; Liu, D.; Liu, S. Transgranular Fracture in Low Temperature Brittle Fracture of High Nitrogen Austenitic Steel. *J. Mater. Sci.* **2007**, *42*, 7514–7519. [CrossRef]

37. Vologzhanina, S.A.; Ermakov, B.S.; Peregudov, A.A. Research of Properties of Cast Austenitic Steels for Low-Temperature Equipment. In *IOP Conference Series: Earth and Environmental Science*; IOP Publishing: Bristol, UK, 2022; Volume 459. [CrossRef]

38. Petrov, Y.N.; Ryzhkov, Y.T. Influence of alloying elements on the structural sensitivity of stacking fault energy in stainless steels. *Metallophysics* **1983**, *5*, 66–70. (In Russian)

39. Narkevich, N.A.; Durakov, V.G.; Surikova, N.S.; Mironov, Y.P.; Mel'nikov, A.G.; Perevalova, O.B.; Shugurov, A.R.; Shulepov, I.A.; Narkevich, V.V. Structure and Lattice Strains in the Surface Cr–Mn–N Steel Layer Formed by a Combination of Friction and Electron-Beam Treatments. *Phys. Met. Metallogr.* **2019**, *120*, 1071–1077. [CrossRef]

40. Sabzi, M.; Farzam, M. Hadfield Manganese Austenitic Steel: A Review of Manufacturing Processes and Properties. *Mater. Res. Express* **2019**, *6*, 1065c2. [CrossRef]

41. Yan, J.-B.; Geng, Y.; Xie, P.; Xie, J. Low-temperature mechanical properties of stainless steel 316L: Tests and constitutive models. *Constr. Build. Mater.* **2022**, *343*, 128122. [CrossRef]